

**GT2011-45180**

## **PROTUBERANCES IN A TURBULENT THERMAL BOUNDARY LAYER**

**Steven R. Mart**  
Graduate Student  
Mechanical Engineering Department  
Baylor University  
Waco, TX 76798-7356

**Stephen T. McClain**  
Assistant Professor  
Mechanical Engineering Department  
Baylor University  
Waco, TX 76798-7356

### **ABSTRACT**

Recent efforts to evaluate the effects of isolated protuberances within velocity and thermal boundary layers have been performed using transient heat transfer approaches. While these approaches provide accurate and highly resolved measurements of surface flux, measuring the state of the thermal boundary-layer during transient tests with high spatial resolution presents several challenges. As such, the heat transfer enhancement evaluated during transient tests are presently correlated to a Reynolds number based either on the distance from the leading edge or on the momentum thickness. Heat flux and temperature variations along the surface of a turbine blade may cause significant differences between the shapes and sizes of the velocity and thermal boundary layer profiles. Therefore, correlations are needed which relate the states of both the velocity and thermal boundary layers to protuberance and roughness distribution heat transfer. In this study, a series of three experiments are performed for various freestream velocities to investigate the local temperature details of protuberances interacting with thermal boundary layers. The experimental measurements are performed using isolated protuberances of varying thermal conductivity on a steadily-heated, constant flux flat plate. In the first experiment, detailed surface temperature maps are recorded using infrared thermography. In the second experiment, the unperturbed velocity profile over the plate without heating is measured using hot-wire anemometry. Finally, the thermal boundary layer over the steadily heated plate is measured using a thermocouple probe. Because of the constant flux experimental configuration, the protuberances provide negligible heat flux augmentation. Consequently, the variation in protuberance temperature is investigated using the velocity boundary layer parameters, the thermal boundary layer parameters, and the local fluid temperature at the protuberance apices. A

comparison of results using plastic and steel protuberances illuminates the importance of the shape of the thermal and velocity boundary layers in determining the minimum protuberance temperatures.

### **INTRODUCTION**

Heat transfer from protuberances is an important phenomenon with implications for both in-flight ice accretion on aircraft [1] and the deposition of combustion impurities on turbine blades. As gas turbine engines operate, they ingest large quantities of air. Given the environment of their operation, this air can contain numerous sources of roughness generating particulates including dust, salt spray from turbines operating in saltwater environments, sand, pollen, or volcanic ash [2]. Additionally, combustion byproducts from dirty, ash producing fuels (especially in land-based power turbines where a broader range of fuel qualities are used [3]), rust, or oil leaks from inside an engine can also serve as a means of roughness formation [2]. During the early stages of roughness formation caused by fuel and foreign matter deposition, the initial deposits resemble isolated elements as opposed to roughness distributions [4]. While the protuberance stage of roughness formation may not last for a long time relative to the total blade life, the presence of the protuberances on the blade surface 1) significantly affects the blade drag, 2) increases the rates of heat transfer from the combustion products to the blade, and 3) creates significant temperature variations along the surface of the blade leading to thermal stresses. The amount and significance of the temperature variations on blade thermal stresses depends on the substrate material of the blade, the thermal conductivity of the roughness elements, and the height above the blade surface to which the protuberance extends into the boundary layer. Evaluating the importance of each of the preceding parameters requires investigating heat transfer from

protuberances and roughness distributions with sufficient resolution to resolve local protuberance temperatures.

The first attempt to understand the heat transfer mechanisms on the scale of a protuberance or roughness element was performed by Henry et al. [1]. Henry et al. [1] used an infrared camera to investigate the temperature changes along isolated plastic hemispherical segments in laminar and turbulent flow. The elements of Henry et al. were attached to a flat plate which was heated using infrared heat lamps. For all but one protuberance investigated, the reduced results of Henry et al. [1] showed that the maximum local heat transfer enhancement increased as the freestream velocity increased. However, Henry et al. made two critical assumptions for their data reduction: internal conduction through the elements was negligible and radiation from the elements to the ambient was negligible. Further, Henry et al. [1] did not report any measured boundary layer quantities. All of the information reported by Henry et al. [1] was presented in comparison to correlation estimates of the velocity boundary layer quantities based on Reynolds number calculated using the distance from the plate's leading edge to the protuberances.

McClain et al. [5] used an extended-surface, discrete element (ES-DEM) analysis to demonstrate that the elements studied by Henry et al. [1] were exhibiting a “fin-like” behavior. Consequently, the enhancements reported by Henry et al. [1] were not true values of convective flux enhancement because of the fin-like nature of the protuberances. Using their one-dimensional modeling approach, McClain et al. [5] also demonstrated that Henry's neglected effects of internal conduction in the protuberance and radiation from the protuberance to the ambient were important. Because the plate used by Henry et al. [1] was heated using infrared lamps with an unknown heat flux, the two separate effects of internal element conduction and element radiation could not be isolated.

McClain et al. [6] employed the discrete-element approach for predicting turbulent convection from roughness distributions to demonstrate that the temperature of the fluid and the thermal conductivity of the roughness elements were important. The thermal conductivity of TBC and fuel deposits are quite different than those of the blade materials. Consequently, the thermal conductivity of the roughness has a significant impact on convective heat transfer rates and therefore, must be considered.

Recently, Bons [7] developed a three-dimensional, transient approach to determine detailed maps of surface flux and Stanton Numbers for rough surfaces based on the one-dimensional method of Schultz and Jones [8]. Bons et al. [9] used the method to measure the flux enhancement on a hemispherical protuberance. The results demonstrated that the 1-D method of McClain et al. [5] and the 1-D method of Schultz and Jones [8] overestimate the flux from the element by failing to capture lateral and internal conduction of the protuberance.

While the approach of Bons [7] is able to provide highly detailed surface maps of heat flux, the transient method does

not allow for easy quantification of the thermal boundary layer quantities which are needed for studies of heat transfer with generalized thermal boundary conditions. In a transient test for flow over protuberances, walls of varying thermal conductivity may be placed upstream of the test section to emulate generalized boundary conditions. During such a test, the flow upstream of the elements initially experiences very high rates of heat transfer. Thus, both the fluid temperature in the boundary layer and the upstream wall flux boundary condition are functions of time. Even with quick response thermocouple beads or cold-wire probes, traversing the boundary layer quickly enough to obtain a “near-instantaneous” thermal boundary layer profile is difficult. Consequently, Bons [7], like Henry et al. [1], was relegated to reporting enhancement values versus the freestream velocities and temperature differences. However, both the fluid velocity profiles and the fluid temperature profiles must be characterized to illuminate the physics of heat transfer enhancement by isolated and distributed roughness elements when exposed to generalized thermal boundary conditions.

To demonstrate the importance of the shape and extents of the thermal boundary layer in determining the heat transfer enhancement of protuberances and roughness distributions, consider the situations presented in **Figure 1**. In the top configuration, a protuberance is attached to an isothermal plate. In the bottom situation, the protuberance is attached to a plate with an unheated starting length. For a fluid with constant properties, the unperturbed velocity profiles at the protuberance position for each situation will be the same; however, the temperature profiles will be vastly different. **Figure 2** shows the unperturbed velocity and temperature profiles at the protuberance location for each situation as evaluated using an educational finite-difference, boundary-layer code for a freestream velocity of 15 m/s using constant fluid properties evaluated for air at 298 K.

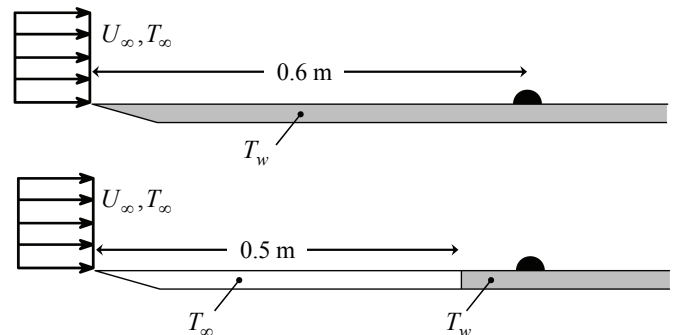


Figure 1. Protuberances on an Isothermal Plate and on a Plate with an Unheated Starting Length (Not to scale)

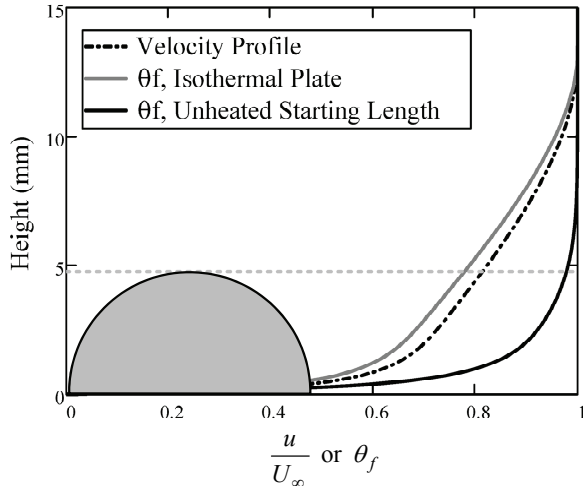


Figure 2. Turbulent Viscous and Thermal Boundary Layer Profiles for Situation

Figure 2 demonstrates that a 9.53-mm diameter hemispherical protuberance would interact with fluid at much different temperatures for each case. Based on an ES-DEM approach, the protuberances on both plates would experience the same local heat transfer coefficients since the velocity profiles are identical. However, for the unheated starting length case, if  $T_w > T_\infty$ , then the protuberance is interacting with much colder fluid than the protuberance on the isothermal wall. While the unperturbed surface flux will increase, a proportional increase in the heat transfer from the protuberance to the fluid is not expected, in general, given the importance of the protuberances thermal conductivity in determining the changes in protuberance temperature along the height of the protuberance.

If the isolated protuberance in Figure 1 were replaced with a roughness distribution, the same arguments would be applicable. That is, roughness distributions on both plates would experience the same velocity profiles, but the temperature profiles of the fluid interacting with the roughness elements would be vastly different for the isothermal case and for the unheated starting length case.

Because turbine engine designers seek to minimize blade thermal stresses caused by changing blade temperatures, changes in thermal boundary conditions along the surface of a gas turbine blade should not be as abrupt as the unheated starting length situation described in Figures 1 and 2. However, because of changes in internal cooling approaches from the leading edge of the blade to the trailing edge [10], changes in the thermal boundary condition will be present along the surface of the blade. Bons [11] also demonstrated that even in a transient facility where the thermal boundary condition is expected to be consistent along the surface, the constant in Reynolds analogy ( $2 \cdot St/C_f = K \approx 1$  for gases) may vary by as much as 35% depending on the level of freestream turbulence intensity or the rate of freestream flow acceleration or deceleration. Given the differences in the velocity gradients

and thermal gradients, as described by the changes in the Reynolds analogy constant, the velocity and thermal boundary layers should not be expected to develop at the same rate or with the same shape. External heat transfer on gas turbine blades is further complicated by the presence of high Mach number flows ( $Ma > 0.7$ ), the presence of shock waves, and the use of film cooling. Each of these situations can change how the thermal boundary layer develops relative to the development of the velocity boundary layer.

Given the need to understand how protuberances and roughness elements behave on surfaces with generalized thermal boundary conditions and given the difficulties in characterizing the thermal boundary layer using transient measurements, this investigation used steady state techniques in order to obtain accurate measurements of the velocity and thermal boundary layer quantities. The objectives of the study were to 1) expand upon the study of Henry et al. for turbulent flow over protuberances by using elements of different thermal conductivities and 2) to investigate the influences of local fluid properties and thermal integral boundary layer quantities on the temperature changes along the heights of the roughness elements.

## METHODOLOGY

To investigate the behavior of protuberances with different thermal conductivities in a turbulent thermal boundary layer, a series of experiments was performed in the Baylor University Subsonic Wind Tunnel (Model 406) which was manufactured by Engineering Laboratory Design, Inc. The wind tunnel test section has a cross-section of 60.96 cm x 60.96 cm (24 in. by 24 in.) and uses a 40 HP electric motor that drives a constant pitch fan. The variable speed motor can produce a flow ranging from a low velocity of 0.1 m/s to an upper tunnel velocity greater than 50 m/s and the velocity variation over the test section is less than  $\pm 1\%$ . An inlet contraction ratio of 6.25:1, a precision honeycomb inlet, and three graduated, high-porosity screens provide a clean inlet turbulence intensity of approximately 0.2%.

The test plate used in this study measured 1.91 cm by 60.96 cm by 91.44 cm (0.75 in. by 24 in. by 36 in.) and was constructed out of Plexiglas. A constant heat flux was applied to the plate with a sheet of gold deposited Mylar film oriented “gold side” down. This orientation allowed for the attachment of protuberances to the insulated side of the Mylar sheet without disrupting the constant flux heating condition it provides. The Mylar sheet used to heat the plate was 30.5 cm wide, started at 1.9 cm from the knife edge, and extended 83.8 cm down the length of the test plate.

A boundary-layer trip was not needed to induce turbulent flow over the plate. Because of the lack of a boundary-layer bleed system and because of the geometry of the knife edge, the flow in the thermal test section of the plate was always turbulent.

Three discrete protuberances of varying thermal conductivity and size were mounted to the test plate. The

protuberances studied were a 9.53 mm hemispherical 316 stainless steel element ( $k_R = 13.4 \text{ W/m}\cdot\text{K}$  [12]), a 9.53 mm hemispherical ABS plastic element ( $k_R = 0.18 \text{ W/m}\cdot\text{K}$ ), and a 5.0 mm hemispherical ABS plastic element. ABS plastic and steel protuberances were used in the study to represent the low end and high end, respectively, of values expected for gas-turbine deposition roughness.

The elements were placed 60 cm from the knife edge of the plate and were spaced 3.81 cm (1.5 in) apart along the span of the plate. The ratio of the protuberance height to the protuberance location from the leading edge was 0.008 for the large protuberances and 0.004 for the small plastic protuberance. These ratios are an order of magnitude larger than the roughness to axial chord ratios expected for erosion or corrosion blade roughness [13], but are representative of the relative roughness heights measured for deposition roughness on land-based high-pressure turbine blades for power generation [3]. Following construction, the plate with protuberances attached was painted with a flat-black paint with a manufacturer reported emissivity of 0.95.

The test plate was mounted in the Baylor University Subsonic Wind Tunnel and a series of three tests were performed. The first set of measurements used a FLIR ThermoCam SC4000 infrared camera to generate highly resolved thermal mappings of the test surface. The SC4000 used in this study has a 320 by 256 pixel resolution indium antimonide (InSb) detector. The accuracy of any surface temperature measurement is reported by FLIR as 0.09 K for temperatures near standard atmospheric conditions [14]. Using a 25-mm lens at a distance from the lens to the heated surface of approximately 36 cm, the width of each pixel represented a width of 0.467 mm on the heated surfaces. This pixel width enabled twenty temperature measurements to be taken across the diameter of the large protuberances and eleven temperature measurements to be taken across the diameter of the small protuberance. The total viewing area of the infrared plate image spanned 14.9 cm in the flow direction and 12.0 cm in the spanwise direction.

The second set of measurements was performed using hot wire anemometry. The unheated velocity boundary layer thickness was acquired over the unperturbed portion of the plate. Finally, a custom fabricated thermocouple probe was used to characterize the thermal boundary layer over the same unperturbed portion of the plate. These three investigations were performed for nominal velocities of 0.7 to 35 meters per second.

For each of these experiments, a Type T thermocouple with an Omega Cold Junction Compensator was used to measure the freestream temperature, a Siemens QFM3101 Relative Humidity Sensor measured the relative humidity in the laboratory, and an Oakton barometer was used to measure the laboratory atmospheric pressure. The freestream velocity was measured using a Pitot-static probe. Because of the large range of velocities tested, a large range of dynamic pressures were measured. Therefore, two different transducers were used to

measure the dynamic pressure difference experienced by the Pitot probe. For the low velocity tests, an Omega PCL-2A pressure transducer, with a range of 0-2 in. of  $\text{H}_2\text{O}$ , a repeatability of 0.0004 in. of  $\text{H}_2\text{O}$ , and an absolute accuracy of .0012 in. of  $\text{H}_2\text{O}$ , was used. For tests over 20 m/s, a Mamac Systems PR-274-R3-VDC pressure transducer was used to measure the dynamic pressure.

For the infrared measurements and the thermal boundary layer tests, an Omega Cold Junction Compensator with a Type K thermocouple was used to measure the temperature of the Plexiglas plate directly below the roughness elements on the underside of the Plexiglas plate. A Newport HHM290 TrueRMS Supermeter measured the voltage supplied to the test plate, and a Fluke Y8100 DC/AC Current Probe (2% absolute accuracy) measured the current supplied to the test plate. With the exception of the Oakton Barometer, Newport HHM290 TrueRMS Supermeter, and Fluke Y8100 DC/AC Current Probe, all of the measurements were acquired using a Dell Optiplex GX260 computer with National Instruments (NI) LabVIEW 7.1 software and a PCI-6052 E Multifunction DAQ card.

Figure 3 presents a side view of the wind tunnel test section and indicates the locations of the protuberances, the infrared camera, and the hot-wire and thermocouple probes relative to the knife-edge of the test plate. The following sections discuss the experimental methods and procedures of each test.

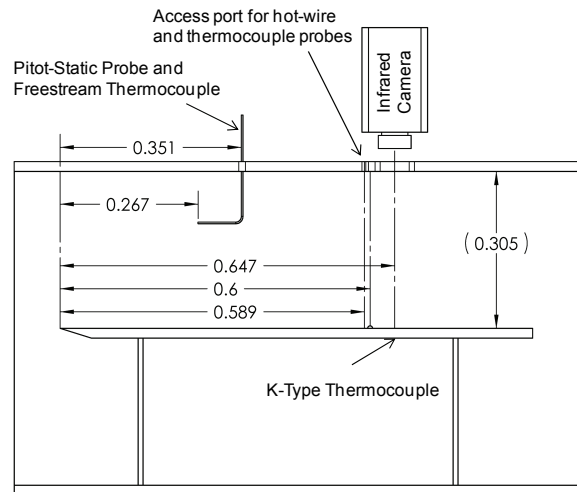


Figure 3. Side View of Wind Tunnel Test Section (all dimensions in meters)

#### Surface Temperature Maps

For this set of tests, the FLIR SC4000 infrared camera was used to monitor the surface temperature of the test plate. To minimize any radiative effects from the lights within the room, the test section was covered with black felt. As mentioned previously, the dynamic pressure, relative humidity, freestream temperature, and Plexiglas temperature were acquired continuously using a LabVIEW driven data acquisition system

measuring 10,000 samples at a rate of 200,000 samples per second. The average value and random uncertainty for each of these measurements were written to a summary file.

An *in-situ* calibration was used to reference the freestream thermocouple and the Plexiglas thermocouple to the infrared camera measurement of an unheated plate temperature in ambient laboratory conditions. To begin the process, a 100-frame, one-point correction was performed using the infrared camera software. Then, a two second infrared video at 30 frames per second was acquired while simultaneously sampling from the freestream thermocouple and the thermocouple attached to the bottom of the Plexiglas plate. The difference between each of the thermocouple measurements and the mean infrared temperature measurement during the calibration period was subtracted from respective thermocouple measurements during the tests. This procedure was performed prior to each day of testing.

Following the *in-situ* calibration, the plate was heated using three BK Precision 1761 power supplies wired in parallel. Starting with a wind tunnel velocity of 0.7 m/s, the plate's temperature was monitored. The settings on the power supplies were set to provide a temperature difference between the plate and the freestream of approximately 15 K. Then, every 10 minutes, an infrared video of the roughness elements was taken for two seconds at a rate of 30 frames per second and the power settings and atmospheric pressure were recorded manually. Once steady state conditions were confirmed by comparing the change in the measured mean surface temperature to the uncertainty in the temperature measurement, a final infrared video was taken. After the final infrared temperature measurement, the wind tunnel velocity was set to the next speed, the settings on the power supplies were adjusted, and the temperature measurement process was repeated.

#### *Velocity Boundary Layer Profiles*

To acquire velocity boundary layer profiles, a Model 1201 hot film probe was powered by a TSI Inc. IFA 300 Constant Temperature Anemometry system. A Dell Optiplex GX1 computer using ThermalPro software was used to initialize the IFA300 and to assign a channel to the probe.

The hot-wire probe was mounted to a Velmex Inc. BiSlide/Unislide assembly used for two-dimensional traversing. The hot-wire probe was positioned 1.1 cm upstream of the protuberances and between the large and small ABS plastic elements. For each boundary layer traverse, the probe was positioned just below the apex of the small plastic element, which was 2.5-mm tall. The Dell Optiplex GX260 computer and LabVIEW 7.1 were used to control and interface with this traversing system.

Starting with a velocity of 0.7 m/s, the traversing system was used to move the probe through a geometrically expanding grid to construct the boundary layer profiles. Once at steady state conditions, the LabVIEW driven stepper motors moved the hot-wire probe through a 6-inch, 101-station, geometrically

expanding measurement grid with a geometric expansion factor of 1.07. Using a United Electronic Industries (UEI) PD2-MFS-4-300/16 PowerDAQ installed on the GX260, 200,000 raw voltages across the probe were sampled at a rate of 200,000 samples per second at each station of the scan. Additionally, 10,000 samples of the dynamic pressure, relative humidity, and freestream temperature were also taken at 200,000 samples per second. Again, the average value and random uncertainty for each of these measurements were written to a summary file. The raw hot-wire voltage measurements at each station were also recorded for post processing.

Atmospheric pressure within the room was recorded at the start and the completion of each trace. Once the scan was completed, the wind tunnel velocity was increased and the process was repeated.

#### *Thermal Boundary Layer Profiles*

To acquire thermal boundary layer profiles, a temperature probe was created using a 30-gage, Type T thermocouple with an Omega Cold Junction Compensator. The thermocouple bead diameter is approximately 0.7 mm (0.03 in). The thermocouple probe was mounted to the Velmex Inc. traversing system discussed in the previous section. The traversing system was used to position the probe at the same starting location used for the velocity boundary layer traces.

An *in-situ* calibration was performed prior to the measurement of the thermal boundary layers which was similar to the method discussed in the surface temperature maps. The test data from the freestream thermocouple, the Plexiglas thermocouple, and thermocouple boundary-layer probe were referenced to unheated ambient conditions that were measured prior to testing after letting the test equipment sit overnight. For the thermal boundary layer calibrations, the freestream thermocouple was taken to be the standard. That is, the difference between the other two thermocouples and the freestream thermocouple during the calibration period was subtracted from the respective temperature measurements during each test.

Starting with a velocity of 0.7 m/s, the test plate was heated and allowed to reach steady state conditions. The settings on the power supplies were matched to those used during the infrared test to ensure similar heating of the plate. Once at steady state conditions, the LabVIEW driven stepper motors moved the probe through the same geometrically expanding measurement grid as was used for the velocity profile measurements. At each point of the scan, the temperature probe acquired 200,000 samples at a rate of 200,000 samples per second. Additionally, 50,000 samples of the dynamic pressure, relative humidity, freestream temperature, and Plexiglas temperature were taken at 200,000 samples per second. The average value and the random uncertainty for each of these measurements were written to a summary file along with the location of the probe. The power settings and atmospheric pressure at the start and finish of each test were recorded manually. Once the trace was completed,

the wind tunnel velocity was increased and the plate was allowed to reach steady state conditions before starting a new scan.

## DATA REDUCTION AND PROCESSING

Each of the measurement sets required unique methods for data reduction. In the following sections, the data reduction methods for each measurement set are described. When available, validations of the measurement methods are also provided.

### Infrared Measurement Processing

The steady state infrared videos and the calibration videos, each of approximately 60 frames, were averaged at each pixel to begin the analysis. While the manufacturer reported uncertainty of any temperature measurement using the camera is 0.09 K, evaluating the mean temperature at each pixel location over the 60-frame steady state video allowed the random uncertainty of each infrared temperature measurement to be reduced to below 0.01 K.

The infrared surface temperature measurements were then processed in a manner similar to that used by Henry et al. [1]. The temperature measurements on the surface regions between the elements were used to evaluate unperturbed surface temperatures for each flow condition. To account for streamwise temperature variations (caused by increasing Reynolds number values) and slight spanwise variations in temperature, a second-order polynomial surface fit was generated using the unperturbed regions of the infrared images. Spanwise variations in the unperturbed regions of the infrared images were on the order of 0.25 K for temperature differences of 15 K between the plate and freestream.

A dimensionless temperature difference was then calculated from Eq. (1) using the measured surface temperature and the unperturbed temperature at each pixel location predicted using the polynomial surface fit.

$$\theta_R = \frac{T_{sur_p} - T_{sur_U}}{T_\infty - T_{sur_U}} \quad (1)$$

**Figure 4** presents a surface contour of the calculated dimensionless temperatures for a freestream velocity of 15 m/s. In **Figure 4**, the flow is from left to right. The large plastic element is at the bottom of the figure, and the steel element is at the top, and the small plastic element is in the middle. **Figure 4** demonstrates the changes in temperature along each of the protuberances, the regions of enhanced heat transfer downstream of the protuberances, and the unperturbed regions of the heated test section.

To further validate the heated plate and temperature measurement systems, the average convection coefficient on the unperturbed regions was determined using Eq. (2).

$$\bar{h} = \left( \frac{\frac{E \cdot I}{A_p} \frac{t_p}{k_p} - (T_M - T_P)}{(T_M - T_P)} \right) \left( \frac{t_M}{k_M} + \frac{t_P}{k_P} \right)^{-1} - \frac{\varepsilon \sigma (T_M^4 - T_\infty^4)}{(T_M - T_\infty)} \quad (2)$$

Eq. (2) corrects for the conduction through the Plexiglas plate, the conduction through the Mylar sheet, and the radiation from the heated surface to the ambient surroundings [15]. For the experiments, the conduction through the Plexiglas and the radiation to the surroundings are important. At the high freestream velocities studied, 10% of the energy dissipated by the gold foil exits through the Plexiglas, while 5% of the energy dissipated by the gold foil leaves as radiation from the plate. For the low freestream velocities, these effects become increasingly important because of the lowered convection coefficients. For the lowest freestream velocity studied (0.7 m/s), 30% of the energy dissipated by the gold foil exits through the Plexiglas, while 37% of the energy leaves as radiation.

The uncertainties of the measured convection coefficients were determined using the large sample size approach of Coleman and Steele [16] which has its origin in the method of Kline and McClintock [17]. **Table 1** presents the uncertainties in the measured quantities used to determine the average convection coefficients determined using Eq. (2).

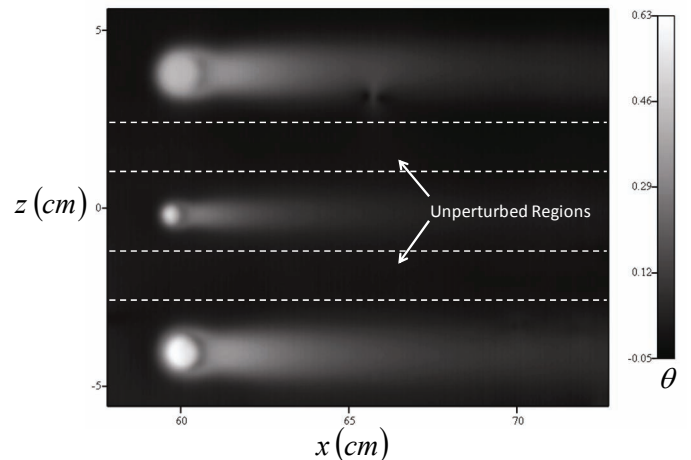


**Figure 4.** Dimensionless Surface Temperatures for the 15 m/s Case

**Figure 5** presents the measured heat transfer coefficients on the unperturbed regions of the plate in the form of Frossling numbers where,

$$Fr_x = \frac{Nu_x}{\sqrt{Re_x}} \quad (3)$$

**Figure 5** further presents a comparison of the measured Frossling numbers to the values predicted by traditional

constant-wall flux Nusselt number correlations for turbulent flow (Eq. 4) and for laminar flow (Eq. 5) neglecting the unheated starting length [18].

$$\text{Nu}_x = 0.0308 \text{Re}_x^{4/5} \text{Pr}^{1/3} \quad (4)$$

$$\text{Nu}_x = 0.453 \text{Re}_x^{1/2} \text{Pr}^{1/3} \quad (5)$$

The unheated starting length correction factor for turbulent flow,  $\left[1 - (x/\xi)^{9/10}\right]^{1/9}$ , is 0.995 at the center of the IR imaging test section for the experimental configuration. Thus, the unheated starting length has a negligible effect on test section convection.

Table 1. Measurement Uncertainties Employed in the Evaluation of Heat Transfer Coefficient Uncertainties

Var.	Instrument	Uncertainty
$T_\infty$	T-type thermocouple	$\left(\left(\frac{tS_{T_\infty}}{\sqrt{N}}\right)_{\text{meas}}^2 + \left(\frac{tS_{T_\infty}}{\sqrt{N}}\right)_{\text{cal}}^2 + \left(\frac{tS_{T_M}}{\sqrt{N}}\right)_{\text{cal}}^2 + (0.09K)^2\right)^{0.5}$
$T_M$	FLIR SC4000	$\left(\left(\frac{tS_{T_M}}{\sqrt{N}}\right)_{\text{meas}}^2 + \left(\frac{tS_{T_M}}{\sqrt{N}}\right)_{\text{cal}}^2 + (0.09K)^2\right)^{0.5}$
$T_P$	K-type thermocouple	$\left(\left(\frac{tS_{T_P}}{\sqrt{N}}\right)_{\text{meas}}^2 + \left(\frac{tS_{T_P}}{\sqrt{N}}\right)_{\text{cal}}^2 + \left(\frac{tS_{T_M}}{\sqrt{N}}\right)_{\text{cal}}^2 + (0.09K)^2\right)^{0.5}$
$E$	Newport HHM290	1% of reading
$I$	Fluke Y8100	2% of FS = 0.4 A
$A_p$	Meter stick	2 mm for each dimension
$t_p$	Manuf. Spec.	0.05 mm
$t_M$	Manuf. Spec.	0.003 mm

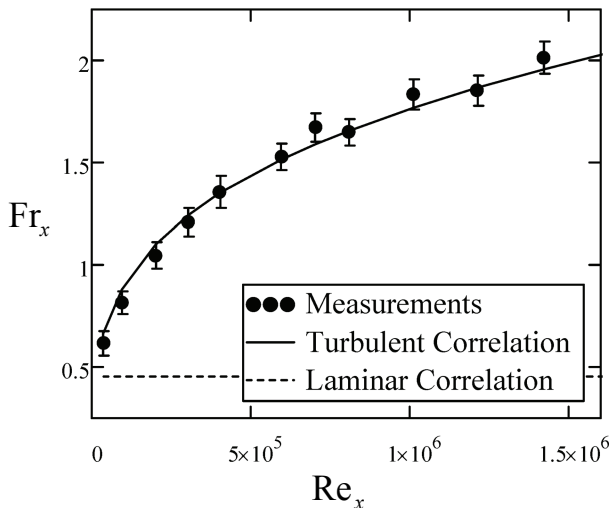


Figure 5. Frossling Number Comparison of the Unperturbed Sections of the Test Plate

Figure 5 demonstrates that with the exception of two flow conditions, the measured Frossling numbers agree with the values predicted by the turbulent correlation. That is, the

uncertainty bars of the measured Frossling numbers includes the values predicted by the correlation. When the uncertainties of the measured Frossling numbers do not include the correlation predictions, the maximum percentage difference between the two is 6% of the correlation value.

#### Velocity Boundary Layer Analyses

A method based on the Clauser approach [19], where points within the overlap region were “best-fit” to the Law of the Wall, was used to simultaneously determine the initial height of the hotwire probe from the plate and the skin friction coefficient for each velocity boundary layer trace. For the Clauser approach, the skin friction coefficient and wall shear are initially estimated for a given profile using the correlation of White [20] for non-accelerating flow over a flat plate.

$$C_f = \frac{0.455}{(\ln(0.06 \text{Re}_x))^2} \quad (6)$$

The velocity profile was transformed to an inner-variable profile, and points within the overlap region ( $80 < y^+ < 200$ ) are identified. A *Given-Minimize* function was then implemented using Mathcad that identified the wall shear and the initial probe height offset that minimized the root-mean-square of the error between the profile overlap points and the expression

$$u^+ = \frac{1}{\kappa} \ln(y^+) + B \quad (7)$$

where  $\kappa = 0.41$  and  $B = 5.0$ . If the points initially identified as being within the overlap subsequently fall outside the overlap region, the method was repeated with the new subset of points within the overlap region.

The Clauser method is very sensitive to the correct selection of points within the overlap region. Based on a perturbation study with the 10 m/s and 15 m/s profiles, the uncertainty in Clauser method is estimated at 5% for both the wall shear and the initial probe offset height for the 2.5 to 30 m/s cases. The uncertainties in the 2.5 to 35 m/s cases is slightly larger than the expected uncertainties for the modified Clauser approach when implemented using a miniature x-wire probe or an LDV system [21].

For the 0.7 m/s case, the logarithmic region is so compressed and the uncertainties in the velocity measurement are so large, because the measurements are at the very limits of the hot-wire calibration range, that the experimental uncertainty is assessed as 15%. While the uncertainty in the 0.7 m/s case is comparatively large to the other velocity cases, the measurements at 0.7 m/s are still presented because of an important flow feature observed in the infrared temperature measurements.

**Figure 6** presents the measured skin friction coefficients evaluated using the Clauser method. The resulting inner variable plots for all of the profiles are presented in **Figure 7**. The Spalding representation of the inner law region [22]:

$$y^+ = u^+ + e^{-\kappa B} \left[ e^{\kappa u^+} - 1 - \kappa u^+ - \frac{(\kappa u^+)^2}{2} - \frac{(\kappa u^+)^3}{6} \right] \quad (8)$$

is also presented in Figure 7 for comparison.

Figures 6 and 7 demonstrate turbulent boundary layer behavior. While differences between the measured  $C_f$  values and the correlation  $C_f$  values are larger than the experimental uncertainties, these differences are explained by the knife-edge condition. Without a boundary-layer suction system or a discrete boundary-layer trip system, the flow adjustment at the leading edge causes the boundary-layer upstream to appear as though it has traveled slightly farther from the leading edge than its actual distance. Thus, the measured skin friction coefficients are less than the correlation would predict, and the difference is more significant at the lower freestream velocities.

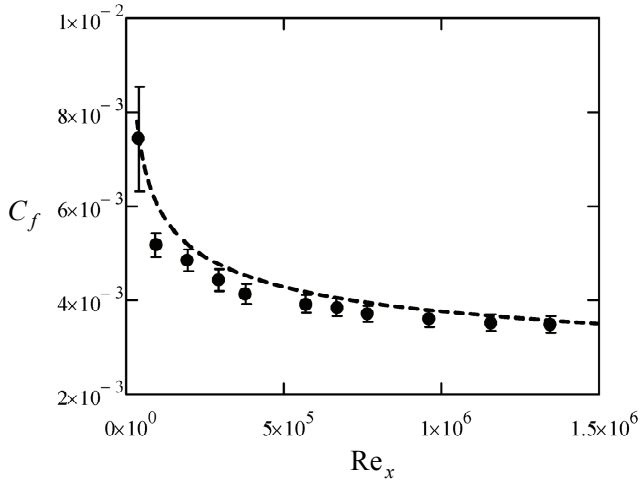


Figure 6. Measured Skin Friction Coefficients versus Reynolds Number

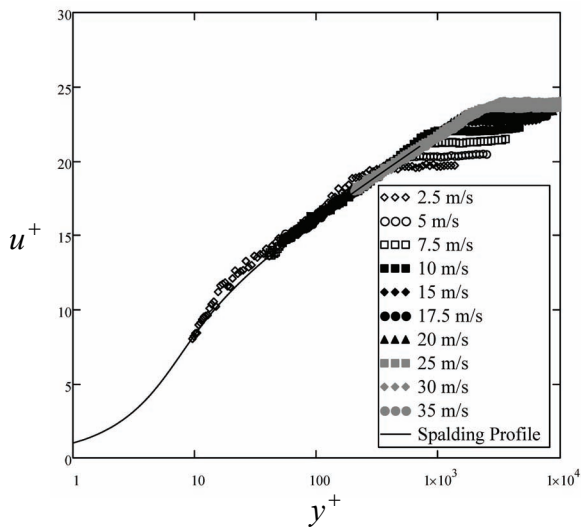


Figure 7. Measured Velocity Profiles Cast in Inner Region Coordinates

### Thermal Boundary Layer Analyses

A method similar to the Clauser method was used to determine the initial offset of the thermal boundary layer profiles. During the thermocouple traces, infrared measurements of the surface could not be made because of interference between the infrared camera and the traversing system. For each thermal boundary layer trace, Eq. (4) was used to determine the convection coefficient. The convection coefficient was used with Eq. (2) to determine the wall temperature during each thermal boundary layer trace based on the measured electrical power dissipated by the plate, the freestream temperature, and the temperature on the Plexiglas plate bottom surface. The correlation convection coefficient and the wall temperature were then used to evaluate the convective flux from the surface.

Employing the previously determined wall shear, the thermal inner variable was evaluated from

$$T^+ = \frac{(T_M - T_f)}{T^*} \quad (9)$$

Mathcad was employed to determine the temperature profile offset height that minimized the error between the points in the thermal overlap region and the thermal overlap region expression:

$$T^+ = \frac{\text{Pr}_t}{\kappa} \ln(y^+) + A(\text{Pr}) \quad (10)$$

where

$$A(\text{Pr}) = 13 \text{Pr}^{\frac{2}{3}} - 7 \quad (11)$$

reported by White [19]. The resulting thermal inner variable plots for the 2.5 to 35 m/s profiles are presented in **Figure 8**.

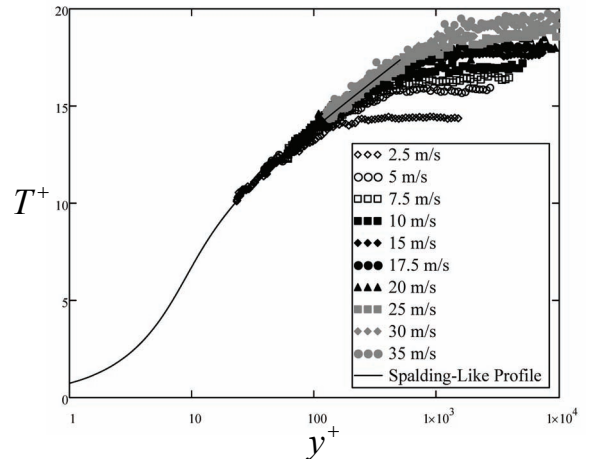


Figure 8. Measured Temperature Profiles Cast in Inner Region Coordinates

Figure 8 also includes a representation of the thermal inner region similar to the Spalding expression, Eq. (8), for the velocity inner region of the boundary layer. Eq. (12) smoothly

merges the thermal conduction sublayer, described by  $T^+ = \text{Pr} y^+$ , with the thermal overlap region described by Eq. (10).

$$y^+ = \frac{T^+}{\text{Pr}} + e^{-\frac{\kappa T^+}{\text{Pr}_t}} \left[ e^{\frac{\kappa T^+}{\text{Pr}_t}} - 1 - \frac{\kappa T^+}{\text{Pr}_t} - \frac{1}{2} \left( \frac{\kappa T^+}{\text{Pr}_t} \right)^2 - \frac{1}{6} \left( \frac{\kappa T^+}{\text{Pr}_t} \right)^3 - \frac{1}{24} \left( \frac{\kappa T^+}{\text{Pr}_t} \right)^4 \right] \quad (12)$$

Eq. (12) is presented in Figure 8 using  $\text{Pr}_t = 0.9$ .

### Derived and Integral Boundary Layer Properties

Once the initial profile offset heights were determined for both the velocity and thermal profiles, the 99% boundary layer thicknesses ( $\delta$  and  $\delta_T$ ) were determined. The integral boundary layer parameters ( $\delta^*$ ,  $\delta_M$ ,  $\delta_T^*$ , and  $\delta_H$ ) were determined using Eqns. (13)-(16).

$$\delta^* = \int_{y=0}^{y=\delta} \left( 1 - \frac{u}{U_\infty} \right) dy \quad (13)$$

$$\delta_M = \int_{y=0}^{y=\delta} \frac{u}{U_\infty} \left( 1 - \frac{u}{U_\infty} \right) dy \quad (14)$$

$$\delta_T^* = \int_{y=0}^{y=\delta_T} \left( \frac{T_f - T_\infty}{T_{surU} - T_\infty} \right) dy \quad (15)$$

$$\delta_H = \int_{y=0}^{y=\delta_T} \frac{u}{U_\infty} \left( \frac{T_f - T_\infty}{T_{surU} - T_\infty} \right) dy \quad (16)$$

The parameter  $\delta_T^*$ , described by Eq. (15), is referred to in this paper as the temperature thickness. Because the energy boundary layer equation in integral form involves the enthalpy thickness, described by Eq. (16), the temperature thickness rarely appears in convection analyses. However, a similar term does commonly appear in integral conduction analyses [23]. The temperature thickness is evaluated for this investigation because it is useful in demonstrating the fin-like behavior of the protuberances.

**Figure 9** presents the integral boundary layer parameters and their variation versus the measured local Reynolds number. The heights of the protuberances are also provided in Figure 9 for comparison to the integral boundary-layer quantities.

In addition to the integral boundary layer parameters, the Reynolds number based on the momentum thickness,  $\text{Re}_{\delta_M}$ , the inner variable height evaluated at the apex elevation of the elements,  $k^+$ , and the Reynolds number based on height of the protuberances and the local fluid velocity evaluated at the protuberance apices:

$$\text{Re}_k = \frac{\rho u_k k}{\mu} \quad (17)$$

were determined. While  $\text{Re}_k$  rarely appears in studies of turbulent flow over distributions of roughness elements, the parameter is commonly used in investigations of bypass transition caused by roughness and isolated elements protruding into a laminar flow. To determine  $u_k$ , a fifth-order polynomial interpolation scheme was employed using the ten velocity profile points above the element apices and the ten profile points below the element apices.

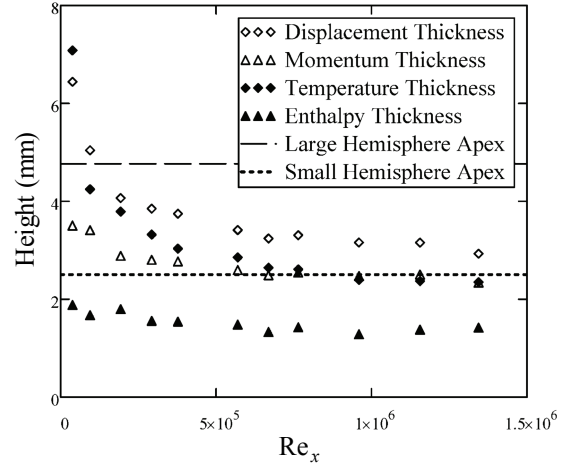


Figure 9. Measured Integral Boundary Layer Quantities and their Variation versus Local Reynolds Number

Further, the dimensionless temperature of the fluid at the apices of the elements was evaluated. As was used for determining  $u_k$ , a fifth-order polynomial interpolation scheme was employed using the ten temperature profile points above the element apices and the ten profile points below the element apices. The dimensionless fluid temperature was then calculated using

$$\theta_f = \frac{T_f - T_{surU}}{T_\infty - T_{surU}} \quad (18)$$

where the unperturbed surface temperature was determined from Eqns. (2) and (4).

**Table 2** presents the calculated velocity and thermal boundary layer parameters for each of the cases studied. Based on the range of  $k^+$  values, Table 2 demonstrates that through the range of tests, the protuberances begin well within the viscous sublayer and conduction sublayer for the 0.7 m/s case and eventually protrude deep within the overlap or logarithmic section of the inner region for the 35 m/s case.

Finally, to compare to the measurements presented here to the work of Henry et al. [1], the apparent enhancement was determined as

Table 2. Summary of Measured Unperturbed Boundary Layer Quantities

$U_\infty$ (m/s)	$Re_{\bar{x}}$	$C_f$	$k_S^+$	$k_L^+$	$Re_{kS}$	$Re_{kL}$	$Re_{\delta_M}$	$\delta$ (mm)	$\delta^*$ (mm)	$\delta_M$ (mm)	$\delta_T$ (mm)	$\delta_H$ (mm)	$\delta_T^*$ (mm)	$\theta_{f,L}$	$\theta_{f,S}$
0.7	39720	0.00744	7	13	17	109	150	27.43	6.44	3.50	26.36	1.88	7.08	0.757	0.628
2.5	91360	0.00518	22	42	274	597	599	37.89	5.04	3.41	21.35	1.67	4.24	0.829	0.723
5	190300	0.00485	40	77	555	1202	926	28.28	4.06	2.88	20.68	1.80	3.79	0.844	0.760
7.5	285800	0.00443	58	110	856	1813	1351	28.03	3.85	2.80	17.64	1.55	3.32	0.850	0.774
10	377500	0.00413	75	143	1160	2437	1803	27.13	3.74	2.77	26.76	1.54	3.03	0.874	0.789
15	578300	0.00391	110	209	1797	3781	2502	28.08	3.41	2.60	22.39	1.48	2.85	0.877	0.805
17.5	677000	0.00384	126	240	2114	4431	2732	27.66	3.24	2.49	17.99	1.33	2.64	0.883	0.805
20	774800	0.00371	140	266	2368	4961	3376	27.80	3.31	2.54	21.37	1.42	2.61	0.885	0.816
25	963100	0.00360	175	333	3066	6388	4140	28.59	3.16	2.47	15.93	1.28	2.39	0.885	0.821
30	1151000	0.00351	208	397	3740	7742	5015	29.50	3.15	2.50	21.31	1.38	2.37	0.896	0.830
35	1344000	0.00348	242	460	4442	9145	5444	28.17	2.93	2.34	16.61	1.42	2.35	0.887	0.832

$$AE_{max} = \frac{T_{sur,U} - T_\infty}{T_{sur,P,min} - T_\infty} \quad (19)$$

While the parameter calculated in Eq. (19) was presented by Henry et al. [1] as the “heat transfer enhancement,” the parameter is not directly related to a change in flux. In fact, for the measurements presented in this study and for the measurements of Henry et al. [1], the heat flux over the test surface is constant. Because of the fin-like behavior of the protuberances, the parameter does not represent a change in the local heat transfer coefficient from the element to the local fluid [5]. The apparent enhancement is merely a dimensionless temperature difference based on the fluid temperature as opposed to the wall temperature as used in Eq. (1).

## RESULTS AND DISCUSSION

The results of the protuberance temperature measurements are presented in four ways. First, the minimum apparent enhancement measurements are presented to compare and contrast the measurements taken in this study to the measurements of Henry et al. [1]. Second, the measurements of surface dimensionless temperature are presented along the centerlines of the elements to demonstrate the effect of element height and thermal conductivity on flow features. Third, the measurements of minimum element temperature are presented versus selected velocity boundary layer quantities. Finally, the variations in the minimum element temperatures are investigated using the thermal boundary-layer features of the flow. **Table 3** presents the measured unperturbed surface convection coefficients, the measured Stanton numbers, and the maximum protuberance normalized temperatures.

### Apparent Enhancement Results

**Figure 10** presents the maximum apparent enhancement values for the protuberances versus the freestream Reynolds number. Figure 10 demonstrates a nearly asymptotic behavior of the apparent enhancement values as the Reynolds number increases. The apparent enhancement values in Figure 10 for the small plastic element (with  $k = 2.5$  mm) of approximately

2.4 at the high end of the Reynolds number range are nearly identical to the values reported by Henry et al. [1] for a similarly sized, plastic spherical segment, with  $k = 2.8$  mm, in turbulent flow. However, the data reported by Henry et al. [1] exhibit a decreasing enhancement with increasing  $Re_x$ . The decreasing enhancement was only identified for the 2.8-mm spherical segment and left unexplained by Henry et al. [1].

Table 3. Convection Coefficient and Protuberance Maximum Normalized Temperature Results

$U_\infty$ (m/s)	$\bar{h}$ $\left(\frac{W}{m^2K}\right)$	$U_{\bar{h}}$ $\left(\frac{W}{m^2K}\right)$	St	$\theta_{LPE}$	$\theta_{SPE}$	$\theta_{SE}$
0.7	4.85	0.50	0.00416	0.374	0.167	0.164
2.5	10.13	0.72	0.00348	0.511	0.366	0.302
5	18.79	1.18	0.00309	0.588	0.466	0.389
7.5	26.68	1.59	0.00292	0.616	0.512	0.425
10	34.37	2.03	0.00285	0.628	0.538	0.437
15	47.93	1.94	0.00267	0.641	0.566	0.455
17.5	56.91	2.30	0.00270	0.658	0.578	0.463
20	60.02	2.37	0.00249	0.659	0.580	0.469
25	74.59	2.95	0.00249	0.669	0.589	0.465
30	82.43	3.18	0.00230	0.663	0.583	0.476
35	97.01	3.81	0.00231	0.679	0.588	0.470

Figure 10 clearly demonstrates the importance of the thermal conductivity of the elements in determining the minimum temperature and maximum apparent enhancement of the protuberances. While the steel element is the same size as the large plastic element, the apparent enhancement is always less than two for the steel element when the apparent enhancement of the large plastic element fluctuates around 3.0. The maximum apparent enhancement of the small plastic element is also significantly higher (asymptotically approaching 2.4) than the steel element even though the height of the small plastic element is nearly half the height of the steel element. Figure 10 demonstrates that the steel element responds very similarly to a plastic element studied by Henry et al. [1] which was almost 1/3 the height of the steel element.

As previously noted, the parameter identified by Henry et al. [1] as an enhancement is not a true flux or convection coefficient enhancement when an object protrudes through the thermal boundary layer. As such, the remainder of this effort focuses on comparisons of the dimensionless protuberance and surface temperatures evaluated using Eq. (1).

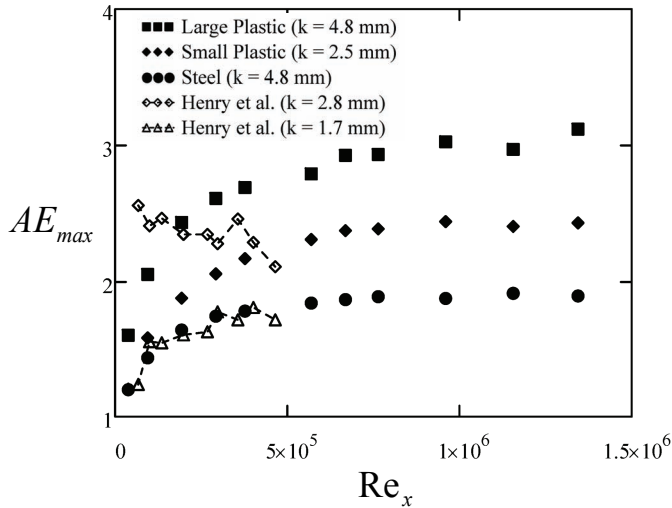


Figure 10: Maximum Apparent Enhancement vs. Reynolds Number

#### Dimensionless Temperature Surface Profiles

Figures 11 and 12 demonstrate how the dimensionless surface temperature profiles ( $\theta_R$ ) are affected by the flow conditions and by the element thermal conductivity. Figure 11 presents surface  $\theta_R$  values for varying freestream velocities along the centerline of the elements grouped by each protuberance. Figure 12 presents surface  $\theta_R$  values along the centerline of the elements grouped by velocity. That is, each subfigure presents a comparison of the protuberance temperatures at a given velocity. For these figures, the element apices are located at an  $x/D_L$  of 0 and the flow is from left to right.

The 0.7 m/s test case is interesting because none of the roughness elements exhibit separated flow characteristics even though the flow over the test plate is turbulent. At this velocity, the flow over the elements can be classified as “creeping” which means that the flow does not form a horseshoe vortex in an upstream stagnation region and that the flow does not separate from the downstream face of the protuberance. Further, the small plastic element continues to demonstrate an interaction with creeping flow for the 2.5 m/s case.

An effect similar to this has been recognized in studies of bypass transition of laminar flow caused by protuberances. For laminar flow over protuberances, an isolated protuberance will cause transition to turbulent flow through a mechanism called bypass transition. Several studies have demonstrated that below a critical value of  $Re_k$ , a laminar flow will not separate from a protuberance and cause bypass transition, [24] and [25]

are examples. Ergin and White identified this critical  $Re_k$  value as 300 [25]. As shown in Table 2, the  $Re_{kS}$  and  $Re_{kL}$  values are both well below this value for the 0.7 m/s case. Figure 11 consequently shows constant  $\theta \approx 0$  values directly behind the protuberances.

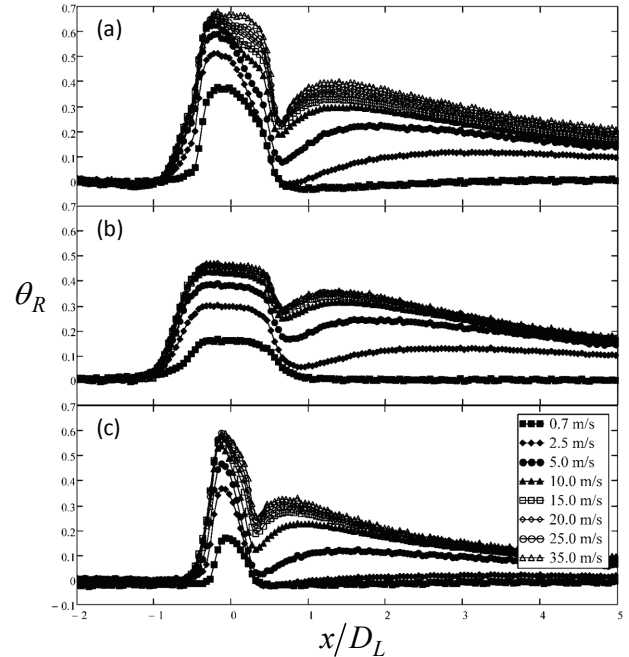


Figure 11: Dimensionless Temperature Values along the Centerline of the (a) Large Plastic Element (b) Steel Element (c) Small Plastic Element

This is also true of the small plastic element at 2.5 m/s. Interestingly, the value of  $Re_{kS}$  for 2.5 m/s (274) is just below Ergin and White’s predicted transition value corresponding to the beginning of bypass transition caused by isolated hemispheres on a flat plate. For the large diameter protuberances at 2.5 m/s, their  $Re_{kL}$  are greater than 300 and the elements trigger flow separation from the downstream element faces. While the fact that a turbulent boundary layer may “creep” over a protuberance is not necessarily surprising, the fact that a critical  $Re_k$  for causing a turbulent boundary layer to separate from a protuberance is so close to the value published for laminar flow is surprising.

For velocities over 2.5 m/s, flow separation exists downstream of all three roughness elements. Downstream of the elements, the right-hand side of Eq. (19) does represent the heat transfer enhancement. Thus, in the wake region

$$\frac{St_P}{St_U} = \frac{T_{sur_U} - T_\infty}{T_{sur_P} - T_\infty} = (1 - \theta_R)^{-1} \quad (20)$$

Figure 11 shows that once the flow separates from the protuberances, directly behind the elements ( $x/D \approx 0.7$ ), the enhancement is low and the normalized surface temperatures are quite high. However, further downstream the flow

reattaches, reintroducing higher heat transfer rates and lowering the plate temperatures. This effect is manifested in the decrease in  $\theta_R$  directly behind the elements and then the rapid increase in  $\theta_R$  as the downstream distance increases.

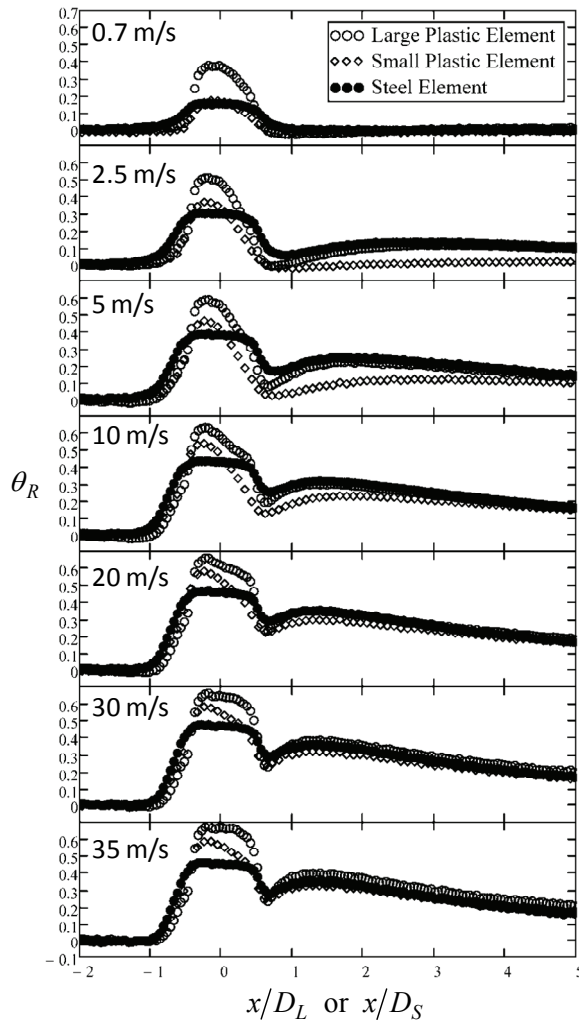


Figure 12: Dimensionless Temperature Values along the Centerline of Each Roughness Element for Varying Velocities

As the velocity increases, the separated regions directly behind the protuberances become less pronounced as the separation bubble is compressed. This is observable in Figure 11 from two effects: 1) the increasing values of  $\theta_R$  in the separation region behind the protuberances and 2) the upstream movement of the maximum  $\theta_R$  values in the wake regions toward the protuberances.

The effects of thermal conductivity are also evident in these two figures. At all speeds, the steel roughness element exhibits near uniform surface temperatures due to its very high thermal conductivity. For the large plastic element, the effects of the low thermal conductivity of the ABS is clearly shown for velocities of 10 m/s and less. The temperature profiles at these speeds show a peak in the value of  $\theta_R$  that declines immediately

downstream of the element apex. Internal conduction near the apex is dictating the surface temperatures of the element resulting in this effect. However, for velocities over 10 m/s, each velocity increase shows an increased “filling out” of the large plastic element’s profile. Figures 11(a) and 11(c) shows this progression. These filling effects are also evident in the small plastic element’s profile. However, due to its small diameter, testing velocities were never great enough for the local convection coefficients to induce slender-fin behavior.

The “filling out” of the  $\theta_R$  surface profile for the large plastic protuberance is caused by the increases in the local protuberance heat transfer coefficient and its gradual dominance over the effects of internal conduction. At 35 m/s, even though the thermal conductivity of ABS plastic is substantially less than that of steel (0.18 versus 13.4 W/m-K), both large elements have identical trends in their profiles and show near uniform surface temperatures across each element. Figure 12 shows this trend as well. Since the Biot number,  $Bi = hD/k_R$ , is increasing as the freestream velocity increases, this does not mean that the large plastic protuberance is not maintaining internal conduction. The behavior implies that the significant internal gradients are pushed to the base of the large plastic element. Consequently, the large plastic element is behaving more as a slender “fin” where the dominant temperature gradients are in the wall-normal direction as the freestream velocities increase.

Figure 12 reemphasizes the effects identified in Figure 11 and further indicates the effect of element thermal conductivity on the protuberance wake region enhancement. Up to freestream velocities of 20 m/s, the maximum wake dimensionless temperature and its location from the protuberance apices is essentially the same for the steel and the large plastic protuberances. However, once the local convection coefficients begin “filling out” the plastic element temperature profile, the maximum wake  $\theta_R$  values begin increasing for the large plastic protuberance.

#### Influence of Velocity Boundary Layer Quantities

**Figure 13** presents  $\theta_{max}$  values, which are the maximum values of  $\theta_R$  on the protuberance, as functions of the local freestream Reynolds number. Figure 13, as was the case for the apparent enhancements of Figure 10, demonstrates that the maximum protuberance dimensionless temperatures increase towards an asymptotical limit. At low Reynolds numbers, the effects of internal conduction are important and impact the surface temperatures of the elements. However, once higher Reynolds numbers are reached, the local heat transfer coefficient dominates causing a longitudinal fin effect and  $\theta_R$  values begin to stabilize.

Figure 9 demonstrates that the integral boundary layer quantities are all decreasing in the manner expected for a fixed plate position, proportional to  $Re_x^n$ , where  $n \approx -1/7$  [19]. As such, the variation in  $\theta_{max}$  is similar versus any of the integral boundary layer parameters. **Figure 14** presents the  $\theta_{max}$  values

versus the measured temperature thickness scaled by the protuberance height. Figure 14 demonstrates that as the velocities increase and the integral boundary layer quantities decrease, the  $\theta_{max}$  values increase linearly until a limit is reached. For the tests over 17.5 m/s, neither  $\theta_{max}$  or  $\delta_T^*/k$  change significantly, resulting in the limiting values.

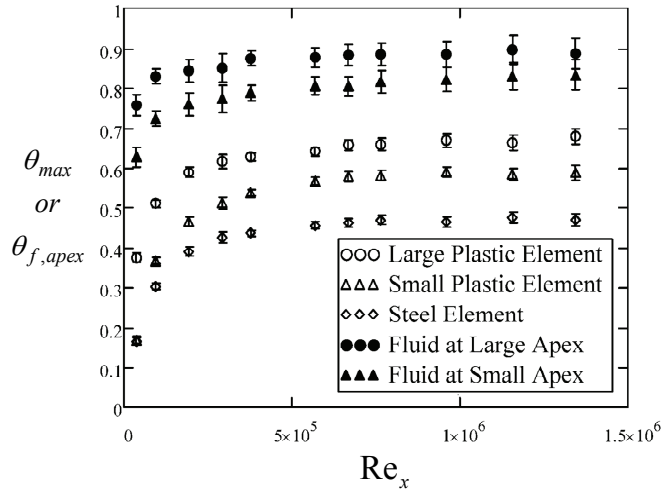


Figure 13. The Maximum Protuberance Dimensionless Temperatures versus the Local Freestream Reynolds Number

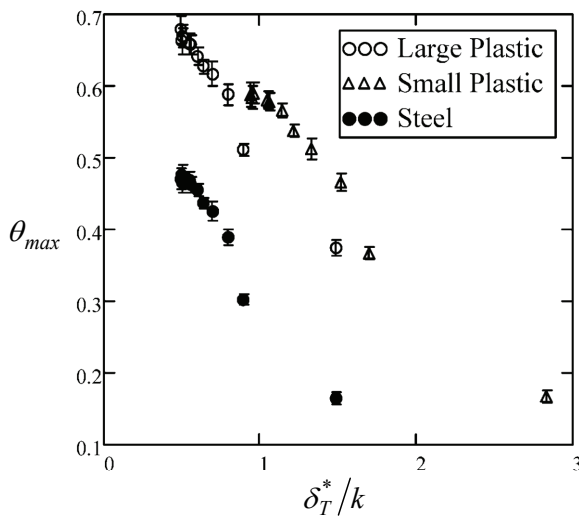


Figure 14. The Maximum Protuberance  $\theta$  Values versus the Temperature Thickness scaled by the Protuberance Height

#### Influence of Thermal Boundary Layer Quantities

Investigating the influence of the local boundary-layer fluid temperature provides insight to the variations exhibited in Figure 14. In addition to the  $\theta_{max}$  values, the values of  $\theta_f$  at the apices of the protuberances are also presented in Figure 13. Figure 13 demonstrates that the  $\theta_{max}$  values are closely following the maximum  $\theta_f$  values of the fluid in contact with the protuberances.

Figure 15 rescales the information of Figure 14 in that  $\theta_{max}/\theta_{f,apex}$  is presented versus the parameter  $(\delta_T^*/k)(Re_k/Re_{kL})^{0.49}$  for the cases that do not exhibit “creeping” flow. The Reynolds number scaling factor for Figure 15 was chosen from the correlation employed by the discrete-element model for predicting the local element convection coefficients [26]:

$$Nu_d = 1.7 Re_d^{0.49} Pr^{0.4} \quad \text{for } Re_d \leq 13,776 \quad (21)$$

where

$$Re_d = \frac{\rho u d}{\mu} \quad (22)$$

and where  $u$  is the local velocity at a given elevation on a protuberance or roughness element. Thus, the new scaling of Figure 15 illuminates the variation in  $\theta_{max}$  values relative to the local fluid temperature,  $\theta_{max}/\theta_{f,apex}$ , and its dependence on the depth that the element protrudes through the thermal boundary layer,  $(\delta_T^*/k)$ , combined with a parameter that corrects for changes in the local protuberance convection coefficients,  $(Re_k/Re_{kL})^{0.49}$ .

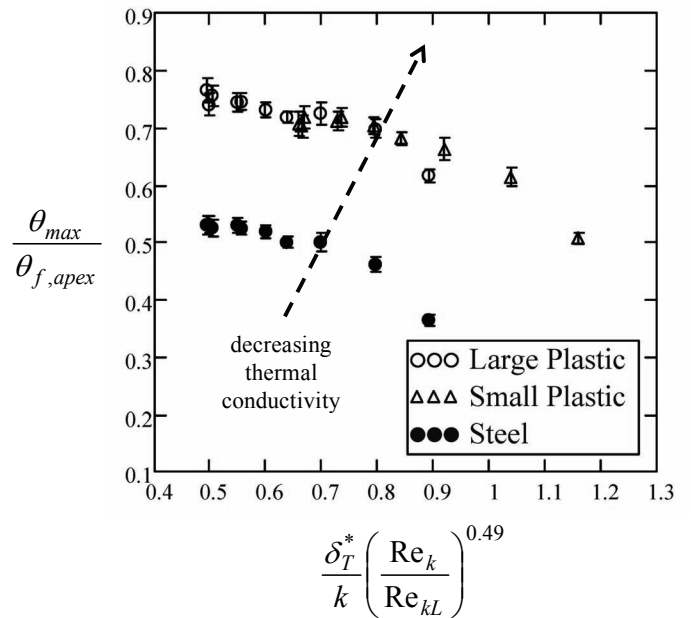


Figure 15. The Variation in the Protuberance  $\theta_{max}$  Values Relative to the Scaled Temperature Thickness Adjusted for Changes in Local Convection Coefficients

Figure 15 demonstrates that the new scaling collapses the behavior of the large and small plastic protuberances. Even though the two protuberances are exposed to different portions of the thermal and velocity boundary layers, the temperature response of the elements to the local boundary layer temperature is related to the product of the element’s relative

height in the thermal boundary layer and the local convection coefficients. While the measurements made in this study were for a configuration where the thermal and velocity boundary layers developed similarly, the element thermal responses captured in Figure 15 for the plastic protuberances demonstrate how both the thermal boundary layer and velocity boundary layer affect protuberance heat transfer.

The objective in adapting the scaling of Figure 14 was to develop a Biot number relationship for the protuberance, such as  $hD/k_R$  or  $hk/k_R$ , that would collapse all of the relative temperature measurements for the fixed protuberance shape. However, when the thermal conductivity is included in the x-axis scaling, the data do not collapse to a single curve. Preliminary steady-state simulations of the protuberance heat transfer indicates that the contact resistance between the Mylar and each protuberance is important.

While all the data do not collapse to a single curve using a Biot number scaling, the collapsing of the plastic protuberances demonstrates how protuberance temperature responds to the shape and height of the thermal boundary layer depending on the local convection coefficients. The presence of the two arcs in Figure 15 also demonstrates the influence of the protuberance thermal conductivity in determining the thermal response of the protuberance. As the thermal conductivity decreases, the arcs shift farther from the origin indicating that the protuberances are more sensitive to the temperature of the local fluid in the boundary layer.

Figure 15 also has significant implications related to the temperatures and thermal stresses experienced by turbine blade surfaces during the beginning stages of roughness deposition. When the deposits are first formed, the temperatures of the elements will be directly related to the height that the elements protrude into the thermal boundary layer. The lower the thermal conductivity of the protuberances and the shorter the thermal boundary-layer is relative to the protuberance height, the more closely the maximum temperature of the protuberances will match the temperature of the fluid at the apex of the protuberances. However, how the  $\theta_{max}$  values affect the base metal temperature and the size of any resulting blade hotspots will be very specific to the blade material, the protuberance material, the internal cooling configuration, the unperturbed surface convection coefficients, and the local protuberance convection coefficients.

Finally, just as the experimental measurements of Bons [9] and Henry et al. [1] do not show the complete picture of protuberance heat transfer, the experimental results presented in this study focus on how the temperatures of protuberances respond to both the thermal and velocity boundary layers depending on the protuberance conductivity. While the average flux (energy dissipation per unit plan-form area of the plate) is assumed to be constant, the details of the local protuberance heat flux were not determined. Two options are available to fully quantify the temperature changes along and the local heat flux variations on a protuberance immersed in a thermal boundary layer. The first involves an inverse-heat

transfer approach employing steady-state simulations where the measured surface temperatures are used as boundary conditions. Alternatively, transient tests similar like those performed by Bons [7] may be used to determine the local surface flux values. Both options for evaluating the local element flux are being pursued.

## CONCLUSIONS

The transient approach of Bons [7] has demonstrated the ability to produce highly resolved maps of the heat transfer coefficients and local Stanton numbers based on the freestream velocity and freestream temperature difference. However, this approach is limited in its ability to measure and relate important thermal boundary layer parameters to the protuberance temperatures given generalized wall thermal boundary conditions. Through the use of steady state measurements, the temperature response of protuberances in thermal boundary layers were characterized in this study.

Using three separate measurement approaches: 1) the temperatures on a heated flat plate along the centerline of the protuberances was characterized, 2) the state of the velocity boundary layer was characterized, and 3) the state of the thermal boundary layer was characterized. The primary observations of the work are:

- 1) The protuberance thermal conductivity was demonstrated to be very important in determining the protuberance temperatures.
- 2) The high thermal conductivity protuberance studied exhibited very little variation in temperature along the protuberance. As was previously noted by Henry et al. [1], the low thermal conductivity protuberances exhibited significant temperature gradients. However, as the freestream velocity increased, the thermal gradients exhibited by the protuberances were predominantly in the wall-normal direction.
- 3) The variations in maximum protuberance dimensionless temperature,  $\theta_{max}$ , were very similar for all of the integral boundary-layer quantities investigated. As the freestream velocity increased, the values of  $\theta_{max}$  increased until they leveled in response to the behavior of the temperature of the fluid at the apices of the elements.
- 4) By scaling  $\theta_{max}$  with the maximum local fluid  $\theta$  and by scaling the relative temperature thickness by the ratio of the local convection coefficients, a relationship between the element temperature, the local fluid temperature, the shape of the thermal boundary layer, and the local convection coefficients was observed based on the collapsing of the results for the plastic protuberances.

Efforts to combine the protuberance thermal response with resolved measurements of local element surface flux are in progress. These efforts involve both steady-state inverse heat transfer simulations and transient experimental measurements based on the approach of Bons [7]. Finally, the measurements made in this study were for a heated plate configuration where the velocity and thermal boundary layers developed similarly. Future efforts are planned to investigate protuberance and roughness distribution heat transfer for situations where the thermal boundary layer development is less dependent on the viscous boundary layer development. These studies will be accomplished using significant unheated starting lengths or the presence of film cooling on the test plates.

## NOMENCLATURE

$A$  = Thermal logarithmic region intercept  
 $A_p$  = Plan form area of heated section of test plate  
 $B$  = Velocity logarithmic region intercept  
 $C_f$  = Skin friction coefficient  
 $c_p$  = specific heat of air  
 $D$  = Protuberance base diameter  
 $d$  = Local diameter of protuberance at a given elevation  
 $E$  = Measured voltage across heating sheet  
 $Fr_x$  = Frossling number based on distance from knife-edge of the plate  $(Nu_x / \sqrt{Re_x})$   
 $\bar{h}$  = convective heat transfer coefficient  
 $I$  = Measured current through heating sheet  
 $k$  = Apex height of protuberance  
 $k_M$  = Thermal conductivity of the Mylar ( $\approx 0.083$  W/m-K)  
 $k_P$  = Thermal conductivity of the Plexiglas (= 0.18 W/m-K)  
 $k_R$  = Thermal conductivity of the protuberance  
 $k_S^+$  = the inner variable height evaluated at the apex of the small plastic element  
 $k_L^+$  = the inner variable height evaluated at the apices of the steel and large plastic elements  
 $N$  = Number of measurements used for to calculate a mean  
 $Nu_x$  = Nusselt number based on distance from knife-edge of the plate  
 $Pr$  = Prandtl number of air at film temperature  
 $Pr_t$  = turbulent Prandtl number  
 $Re_x$  = Reynolds number based on distance from knife-edge of the plate  
 $Re_{\bar{x}}$  = average Reynolds number based on distance from knife-edge of the plate  
 $Re_{kS}$  = Reynolds number at small protuberance apex  
 $Re_{kL}$  = Reynolds number at large protuberance apex  
 $Re_{\delta M}$  = Reynolds number based on the momentum thickness  
 $S$  = Measurement standard deviation  
 $T^+$  = inner variable temperature

$T^*$  = wall conduction temperature,  $\frac{q_{conv}''}{\rho c_p u^*}$   
 $T_M$  = Average unperturbed Mylar surface temperature measured using infrared thermometry  
 $T_P$  = Plexiglass surface temperature  
 $T_{sur.P}$  = local perturbed surface temperature  
 $T_{sur.U}$  = local unperturbed surface temperature  
 $T_W$  = wall temperature  
 $T_f$  = temperature of the fluid  
 $T_\infty$  = temperature of the air far from the surface  
 $t$  = Student's-t value ( $\approx 2.0$ )  
 $t_M$  = Mylar thickness (= 0.185 mm)  
 $t_P$  = Plexiglas thickness (= 19.05 mm)  
 $u$  = component of flow along the primary wind tunnel axis  
 $u^*$  = friction velocity,  $\sqrt{\frac{\tau_w}{\rho}}$  or  $U_\infty \sqrt{\frac{C_f}{2}}$   
 $u^+$  = normalized inner variable velocity ( $u/u^*$ )  
 $u_k$  = velocity at the apex of protuberance (m/s)  
 $U_{\bar{h}}$  = Uncertainty in measured convection coefficient  
 $U_\infty$  = Freestream velocity (m/s)  
 $y^+$  = inner variable height  
 $\alpha$  = thermal diffusivity of air at film temperature ( $m^2/s$ )  
 $\delta$  = viscous boundary layer thickness  
 $\delta^*$  = displacement thickness  
 $\delta_H$  = enthalpy thickness  
 $\delta_M$  = momentum thickness  
 $\delta_T$  = thermal boundary layer thickness  
 $\delta_T^*$  = temperature thickness  
 $\theta_{max}$  = maximum dimensionless temperature  
 $\theta_R$  = Dimensionless temperature over element and surface  
 $\theta_{f,S}$  = Dimensionless temperature of unperturbed fluid at the elevation of the small element apex  
 $\theta_{f,L}$  = dimensionless temperature of unperturbed fluid at the elevation of the large element apex  
 $\kappa$  = von Karman's constant  
 $\rho$  = fluid density  
 $\varepsilon$  = emissivity of the Mylar surface (0.95)  
 $\nu$  = kinematic viscosity of air  
 $\sigma$  = Stefan-Boltzmann constant  
 $\mu$  = molecular viscosity  
 $\xi$  = unheated starting length

## Subscripts

$cal$  = value associated with measurements performed during *in-situ* calibration  
 $LPE$  = Large plastic element  
 $meas$  = value associated with measurements performed during testing  
 $SE$  = Steel element  
 $SPE$  = Small plastic element

## ACKNOWLEDGMENTS

The authors thank Dr. William Jordan and the Mechanical Engineering Department at Baylor University for their support of these activities. The authors also thank Dr. Kenneth Van Treuren, Dr. Lesley Wright, and Mr. Jason Gregg for their valuable input and collaborative efforts throughout this process. Finally, the authors thank Ashley Orr and Gilberto Narvaez III for their help with test plate construction, traversing system automation, and LabVIEW programming.

## REFERENCES

- [1] Henry, R. C., Hansman, R. J., and Breuer, K. S., "Heat Transfer Variation on Protuberances and Surface Roughness Elements", *Journal of Thermophysics and Heat Transfer*, Vol. 9, No. 1, March 1995.
- [2] Bons, J. P., "A Review of Surface Roughness Effects in Gas Turbines", *Journal of Turbomachinery*, Vol. 132, April 2010
- [3] Bons, J. P., Taylor, R. P., McClain, S. T., and Rivir, R. B., "The Many Face of Turbine Surface Roughness", *Journal of Turbomachinery*, Vol. 123, pp. 739-748, October 2001.
- [4] Wammack, J. E., Crosby, J., Fletcher, D., Bons, J. P., and Fletcher, T. H., (2008), "Evolution of Surface Deposits on a High-Pressure Turbine Blade—Part I: Physical Characteristics," *Journal of Turbomachinery*, Vol. 130, 021020.
- [5] McClain, S. T., Vargas, M., Kreeger, R. E., and Tsao, J. C., "Heat Transfer from Protuberances", *Journal of Thermophysics and Heat Transfer*, Vol. 21, No. 2, pp. 337-345, 2007.
- [6] McClain, S. T., Hodge, B. K., and Bons, J. P., "The Effect of Element Thermal Conductivity on Turbulent Convective Heat Transfer for Rough Surfaces", ASME Paper No. GT2009-59458, 2009
- [7] Bons, J. P., (2009), "Transient Method for Convective Heat Transfer Measurement With Lateral Conduction—Part I: Application to a Deposit-Roughened Gas Turbine Surface," *Journal of Heat Transfer*, Vol. 131, 011301.
- [8] Schultz, D. L., and Jones, T. V., (1973), "Heat-Transfer Measurements in Short-Duration Hypersonic Facilities," Advisory Group for Aerospace Research and Development (165). NATO.
- [9] Bons, J. P., Fletcher, D., and Borchert, B., (2009), "Transient Method for Convective Heat Transfer Measurement With Lateral Conduction—Part II: Application to an Isolated Spherical Roughness Element," *Journal of Heat Transfer*, Vol. 131, 011302.
- [10] Han, J.-C., Dutta, S., and Ekkad, S. V., (2000), *Gas Turbine Heat Transfer and Cooling Technology*, New York: Taylor & Francis.
- [11] Bons, J., (2005), "A Critical Assessment of Reynolds Analogy for Turbine Flows," *Journal of Heat Transfer*, Vol. 127, No. 3, pg 472-485.
- [12] Gebhart, B., (1993), *Heat Conduction and Mass Diffusion*, McGraw-Hill, Inc., 1<sup>st</sup> Ed.
- [13] Boyle, R. J., and Senyitko, R. G., (2005), "Effect of Surface Roughness on Turbine Vane Heat Transfer", ASME Paper No. GT2005-68133.
- [14] FLIR, (2010) "ThermoVision® SC4000: Science-Grade Infrared Camera," [www.flir.com](http://www.flir.com).
- [15] Mart, S. R. and McClain, S. T., (2009), "Heat Transfer from Protuberances and Simulated Ice Accretion Roughness Elements," *Proceedings of the 2009 ASME International Mechanical Engineering Congress & Exposition*, November 13-19, Lake Buena Vista, FL, IMECE2009-10825.
- [16] Coleman, H. W. and Steele, W. G., (1999), *Experimentation and Uncertainty Analysis for Engineers*, Second Edition, John Wiley and Sons, Inc.
- [17] Kline, S. J., and McClintock, F. A., (1953), "Describing Uncertainties in Single-Sample Experiments," *Mechanical Engineering*, Vol. 75, pg 3-8.
- [18] Bejan, A., (2004), *Convection Heat Transfer*, Wiley & Sons, Inc., 2<sup>nd</sup> Ed.
- [19] Clauser, F. H., 1954, "Turbulent Boundary Layers in Adverse Pressure Gradients," *J. Aeronaut. Sci.*, 21, pp. 91-108.
- [20] White, F. M., (2006), *Viscous Fluid Flow*, Boston, McGraw-Hill, 3<sup>rd</sup> ed.
- [21] Schultz, M. P. and Flack, K. A., (2003), "Turbulent Boundary Layers Over Surfaces Smoothed by Sanding," *Journal of Fluids Engineering*, Vol. 125, pg 863-870.
- [22] Spalding, D. B., (1961), "A Single Formula for the Law of the Wall," *J. Appl. Mech.*, Vol. 28, pg 455-457.
- [23] Goodman, T. R., (1964), "Application of Integral Methods to Transient Nonlinear Heat Transfer," *Advances in Heat Transfer*, Vol. 1, pg 52-122.
- [24] Klebanoff, P. S., W. G. Cleveland, and K. D. Tidstrom, "On the evolution of a turbulent boundary layer induced by a three-dimensional roughness element," *Journal of Fluid Mechanics*, No. 237, 101-187, 1992.
- [25] Ergin, F. G. and White, E. B., "Multicomponent and Unsteady Velocity Measurements of Transient Disturbances," Presented at the 43rd AIAA Aersospace Sciences Meeting and Exhibit, 10-13 January, 2005, Reno, NV, AIAA 2005-527.
- [26] McClain, S. T., Hodge, B. K., and Bons, J. P., (2004), "Predicting Skin Friction and Heat Transfer for Turbulent Flow over Real Gas-Turbine Surface Roughness Using the Discrete-Element Method," *Journal of Turbomachinery*, Vol. 126, No. 2, pg 259-267.